Jisha Joseph "Self-assembly of structurally diverse phosphomolybdates: synthesis, structure and properties." Thesis. Research and Post gradute Department of Chemistry, St. Thomas college (autonomous), University of Calicut, 2020.

CHAPTER II

Role of supramolecular interactions in crystal packing of Strandberg-type cluster based hybrid solids

Summary

Two new Strandberg-type cluster based phosphomolybdates {H-2*a3mp*}$_5$ [{PO$_3$(OH)}{PO$_4$}Mo$_5$O$_{15}$], **1** and {H-2*a4mp*}$_5$[{PO$_3$(OH)}{PO$_4$}Mo$_5$O$_{15}$].6H$_2$O, **2** have been crystallized *via* solvent evaporation technique using 2-amino-3-methylpyridine (2*a3mp*) and 2-amino-4-methylpyridine (2*a4mp*) respectively. The solids were characterized using single crystal X-ray diffraction, powder X-ray diffraction, fourier transform infrared spectroscopy, thermogravimetric analysis, scanning electron microscopy and cyclic voltammetry. The solid **1** crystallized in monoclinic system with space group *P*2$_1$/*c*, *a* = 8.394(1), *b* = 27.398(6), *c* = 21.521(4) Å, *β* = 97.68(3)°, Z = 4. The solid **2** crystallized in triclinic system with space group *P*-1, *a* = 11.728(1), *b* = 14.234(1), *c* = 19.589(1) Å, *α* = 68.906(3), *β* = 89.454(3), *γ* = 66.559(3)°, Z = 2. The solids **1** and **2** formed a supramolecular framework stabilized by hydrogen bonding interaction between cluster anions and organic moieties. CH…π interactions between the organic moieties reinforced the crystal packing in **1** and **2**. While crystal packing effects resulted in the formation of solvent accessible voids in **1**; aggregation of lattice water molecules in **2** facilitated the formation of pentameric water cluster. The electrochemical behavior of **1** and **2** has been investigated. In addition, the optical band gap energy of the solids have also been calculated using UV-DRS data.

II.1. Introduction

Supramolecular assemblies based on phosphomolybdate (PMO) cluster anions are captivating organic-inorganic hybrid solids on account of their diverse topologies, tuneable size and structural versatility [1,2]. Owing to their unique structural features, they exhibit a wide range of applications in multiple areas such as catalysis [3,4], magnetism [5], ion-exchange [6,7] and electrochemistry [8-10]. Among the PMO cluster anions, Strandberg-type $\{P_2Mo_5O_{23}\}^{6-}$ is the most stable cluster anion that can be crystallized under ambient conditions [11-13]. It was first reported by Strandberg in 1973 [14] and so far several hybrid solids have been reported based on $\{P_2Mo_5\}$ cluster anion with promising properties [15-18]. Majority of these solids have been crystallized along with protonated organic ligands having nitrogen donor atoms [19-21]. Since, $\{P_2Mo_5\}$ cluster anion is stable in the pH range 1-7, organic ligands tend to be protonated (at pH < pK_a) and electrostatic interaction between the organic cations and inorganic polyanions enables the crystallization of hybrid solids. The protonated ligands exhibit hydrogen bonding interactions along with CH…π and/or π…π interactions which leads to the stabilization of the supramolecular aggregates and result in fascinating 3-D networks [22-24].

For the past decade, a few groups have been investigating the role of supramolecular interactions in stabilizing the crystal packing in $\{P_2Mo_5\}$ cluster based solids [25-28]. It was observed that these solids demonstrate remarkable structural characteristics such as porosity, aggregation of water clusters and supramolecular isomerism [28,29]. However, the electrochemical behavior of Strandberg-type cluster based solids is proportionately less investigated. Therefore, in this chapter, an attempt has been made to crystallize hybrid solids based on Strandberg-type $\{P_2Mo_5\}$ cluster, examine the role of supramolecular interactions

in stabilizing the crystal packing in the solids and explore the electrochemical nature of the synthesized solids. Under ambient temperature, $\{H-2a3mp\}_5[\{PO_3(OH)\}\{PO_4\}Mo_5O_{15}]$, **1** and $\{H-2a4mp\}_5[\{PO_3(OH)\}\{PO_4\}Mo_5O_{15}].6H_2O$, **2** were crystallized from an aqueous medium using isomeric ligands *viz.* 2-amino-3-methylpyridine (*2a3mp*) and 2-amino-4-methylpyridine (*2a4mp*) respectively by means of solvent evaporation technique. A detailed structural analysis of the solids revealed the role of H-bonding and CH…π interactions in the self-assembly of **1** and **2**. Moreover, the electrochemical nature of **1** and **2** was explored by means of three electrode system using 1 mM $K_4[Fe(CN)_6]$ in 0.1 M KCl as supporting electrolyte. Previously, electrochemical behavior of $\{P_2Mo_5\}$ cluster based solids has been investigated only in acidic medium [30,31]. This is the first attempt to examine the nature of $\{P_2Mo_5\}$ cluster based solids when $K_4[Fe(CN)_6]$ is used in KCl as supporting electrolyte. The band gap energies (E_g) of the as-synthesized solids were calculated to understand the changes in E_g when monoprotonated cluster anion is surrounded by isomeric ligands.

II.2. Experimental Section

II.2.1. Synthesis

0.4 g of $Na_2MoO_4.2H_2O$ (1.65 mmol, Merck) was dissolved in 20 ml of distilled water and labeled as Solution A. Solution B was prepared by dissolving 0.15 ml of 2-amino-3-methylpyridine (1.47 mmol, Aldrich) in 20 ml of distilled water. Subsequently, Solution B was slowing added to Solution A and kept under stirring for five minutes. Upon stirring a turbid solution was obtained. Thereafter, 1M orthophosphoric acid (H_3PO_4, Merck, 85%) was added drop wise to obtain a clear solution (pH ~ 1) and the resultant solution was left undisturbed for crystallization. After two weeks, needle shaped crystals of **1** were obtained

(Yield: 65-70% based on molybdenum). The crystals were washed with distilled water and acetone and allowed to dry at room temperature.

The same procedure was repeated using 2-amino-4-methylpyridine instead of 2-amino-3-methylpyridine and block shaped crystals of **2** were obtained (Yield: 65-70% based on molybdenum).

II.2.2. Characterization

II.2.2.1. X-ray crystallographic studies

X-ray diffraction studies of crystal mounted on a capillary were carried out on a BRUKER AXS SMART-APEX diffractometer with a CCD area detector (MoKα = 0.71073Å, monochromator: graphite) [32]. Frames were collected at T = 293K (for **1**) and 296K (for **2**) by ω, ϕ and 2θ-rotation at 10s per frame with SAINT [33]. The measured intensities were reduced to F^2 and corrected for absorption with SADABS [33]. Structure solution, refinement, and data output were carried out with the SHELXTL program [34]. Non-hydrogen atoms were refined anisotropically. C-H and N-H hydrogen atoms were placed in geometrically calculated positions by using a riding model. Images were created with the DIAMOND program [35]. Hydrogen bonding interactions in the crystal lattice were calculated with SHELXTL and DIAMOND [34,35]. Crystal and refinement data are summarized in Table II.1.

II.2.2.2. Powder X-ray diffraction (PXRD)

PXRD data was collected on a Malvern Panalytical Aeris diffractometer using Ni-filtered CuKα radiation. Data were collected with a step size of 0.02° and count time of 2s per step

over the range $5° < 2\theta < 60°$.

II.2.2.3. **Fourier transform infrared spectroscopy (FTIR)**

FTIR spectra were recorded on KBr pellets using Shimadzu FTIR spectrophotometer (model: IR Affinity).

Table II.1. Crystallographic details for **1** and **2**.

	1	**2**
Formula	$C_{30}H_{45}Mo_5N_{10}O_{23}P_2$	$C_{30}H_{45}Mo_5N_{10}O_{29}P_2$
Formula weight	1455.40	1551.4
T (K)	293(2)	296(2)
Space Group	$P2_1/c$	P -1
a, Å	8.394(1)	11.728(1)
b, Å	27.398(6)	14.234(1)
c, Å	21.521(4)	19.589(1)
α, °	90.00	68.906(3)
β, °	97.68(3)	89.454(3)
γ, °	90.00	66.559(3)
V, Å^3	4905.1(18)	2765.1(4)
Z	4	2
d_{calc}, g·cm^{-3}	1.971	1.863
$\mu_{MoK\alpha}$, cm^{-1}	1.397	1.254
λ (Å)	0.71073	0.71073
$R_1(I>2\sigma I)$, WR_2(all)	0.0408, 0.1114	0.0391, 0.1153
GOF	1.080	1.111
CCDC No.	1999772	1999773

II.2.2.4. Thermogravimetric analysis (TGA)

TGA was done on Perkin-Elmer TGA7 from room temperature to 900ºC at a heating rate of 10ºC/min. in nitrogen atmosphere to determine water and organic content as well as overall thermal stability of the product.

II.2.2.5. Scanning electron microscopy (SEM)

SEM studies were carried out on crystals mounted on carbon tape using FEI FESEM Quanta 200 at an accelerating voltage of 20 kV.

II.2.2.6. Cyclic voltammetric studies

The electrochemical measurements were carried out on CH1608 electrochemical work station using three-electrode system with saturated Ag/AgCl as the reference electrode and platinum wire as a counter electrode. The working electrode was fabricated by coating solids **1** and **2** separately on glassy carbon electrode (GCE) by simple drop casting method. 1 mM $K_4[Fe(CN)_6]$ in 0.1 M KCl was used as the supporting electrolyte to study the electrochemical properties.

II.2.2.7. Band gap energy calculations

Band gap energy calculations were done using data collected from UV-Vis spectrophotometer (UV-2600 spectrometer, Shimadzu, Japan).

II.3. Results and Discussion

II.3.1. Crystal structure of 1 and 2

The solids **1** and **2** are based on $\{P_2Mo_5\}$ cluster anion which consists of edge and corner sharing MoO_6 octahedra forming a Mo_5O_{15} ring capped by two PO_4 tetrahedra; the anion is identical to the one found in many solids [28].

The crystal structure of $\{H-2a3mp\}_5[\{PO_3(OH)\}\{PO_4\}Mo_5O_{15}]$, **1** and $\{H-2a4mp\}_5[\{PO_3(OH)\}\{PO_4\}Mo_5O_{15}].6H_2O$, **2** suggests the presence of one cluster anion and five monoprotonated ligand moieties per asymmetric unit (Figure II.1). In addition six lattice water molecules per asymmetric unit are present in **2**. Bond valence sum (BVS) calculations [36] indicate that in both **1** and **2**, one of the phosphate groups per cluster anion is protonated (henceforth referred to as $\{HP_2Mo_5\}$). Moreover in both **1** and **2**, $\{HP_2Mo_5\}$ cluster anion exhibits extensive H-bonding interactions with ligand moieties; however, the nature of supramolecular interactions in **1** and **2** is quite different.

In **1**, protonation of terminal oxygen i.e. O22 on the phosphate group results in a strong H-bonding interaction (2.411(12) Å) between P=O and P-OH groups of neighboring clusters thereby dictating the formation of 1-D chains of $\{HP_2Mo_5\}$ cluster anions as shown in Figure II.2a. While, four of the $\{H-2a3mp\}^+$ moieties *viz.* {N3N4}, {N5N6}, {N7N8} and {N9N10} are connected to $\{HP_2Mo_5\}$ cluster anion through NH…O interactions; the fifth $\{H-2a3mp\}^+$ moiety i.e. {N1N2} also links the adjacent $\{HP_2Mo_5\}$ cluster anions through CH…O interactions to form 1-D chains (Figure II.2b). H-bonding interactions in **1** have been summarized in Table II.2. The 1-D chains are further linked via {N9N10} moieties through H-bonding (N9H9C…O8: 2.324(24) Å) interaction to form 2-D zig-zag sheet. The

formation of 2-D sheets is also reinforced by $\pi\ldots\pi$ interactions (3.551(5) Å) mediated by {N7N8} and {N9N10} moieties of neighboring 1-D chains (refer Figure II.2c). The packing of 2-D sheets is facilitated by CH$\ldots\pi$ interactions as shown in Figure II.3. It is noteworthy that the structure showed solvent accessible voids of diameter 3.8 nm (refer Figure II.3c).
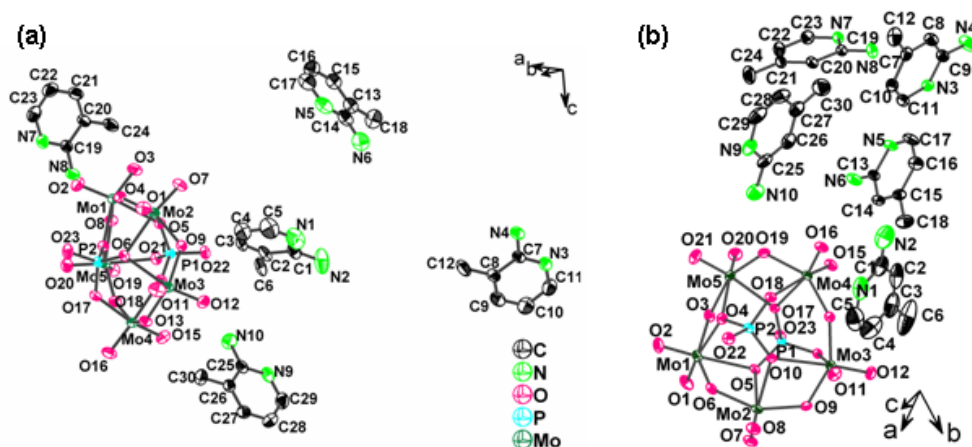

Figure II.1. An ORTEP view of (a) **1** and (b) **2**. The lattice water molecules in **2** have been removed for clarity.

Table II.2. Hydrogen bonding interactions in **1**.

D-H…A	D-H (Å)	H…A (Å)	D…A (Å)	∠ D-H…A (°)
N3-H3C…O17	0.861(8)	2.073(5)	2.874(11)	154.36(22)
N4-H4A…O23	0.860(9)	2.123(15)	2.969(23)	167.95(23)
N6-H6A…O21	0.859(10)	2.226(19)	3.076(29)	169.87(28)
N5-H5C…O1	0.86(1)	1.892(17)	2.691(28)	153.91(25)
N8-H8B…O4	0.860(4)	1.960(17)	2.798(20)	164.61(23)
N8-H8A…O22	0.860(14)	2.134(27)	2.956(42)	159.82(21)
N9-H9C…O13	0.860(14)	1.838(29)	2.680(44)	165.52(20)
N10-H10A…O17	0.860(14)	2.239(22)	3.050(37)	157.20(24)
N10-H10B…O15	0.859(6)	2.214(3)	2.956(5)	144.55(24)
C6-H6F…O22	0.961(4)	2.229(5)	3.094(10)	149.12(21)
C6-H6D…O8	0.960(15)	2.036(35)	2.978(50)	166.62(23)
C3-H4C…O9	0.931(3)	1.833(2)	2.713(4)	156.75(22)
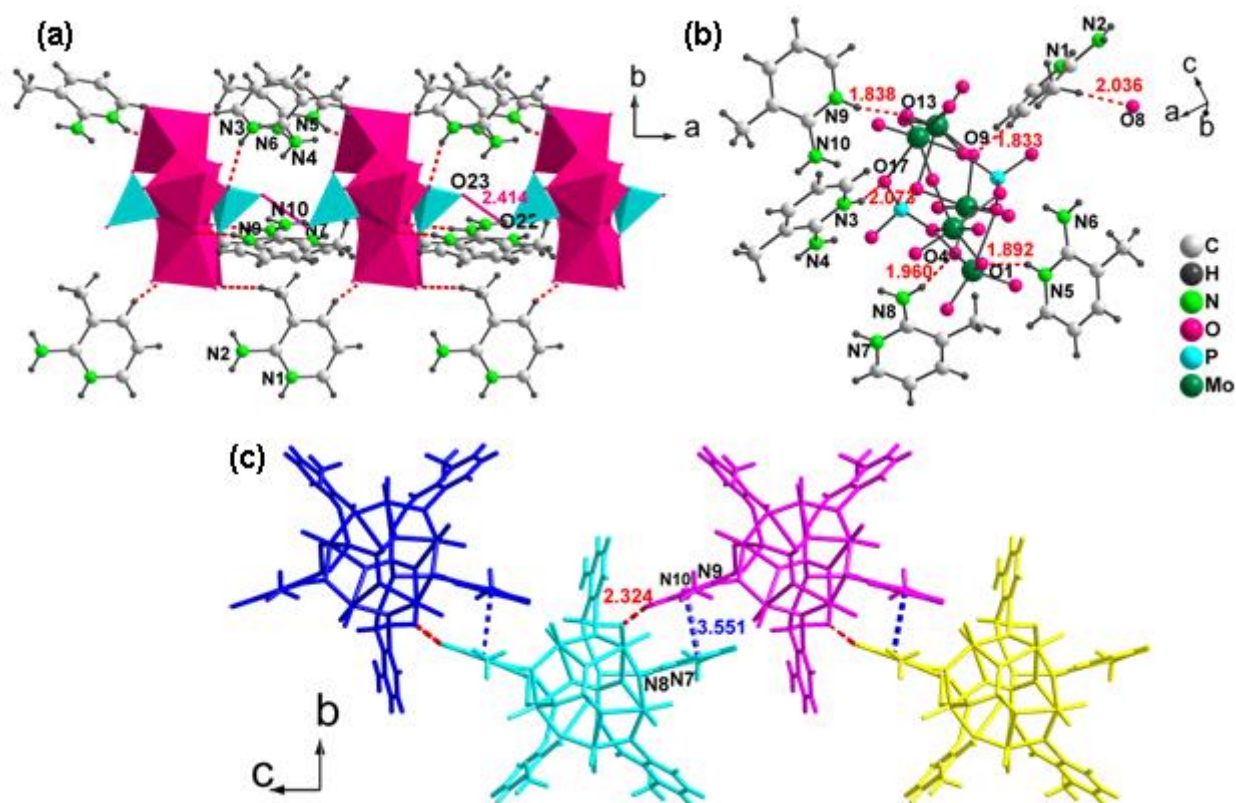
Figure II.2. (a) 1-D chains in **1** mediated by O…O interactions (shown in solid red lines) between terminal oxygen atoms O22 and O23 of phosphate groups of neighboring cluster anions. Formation of 1-D chains is also facilitated by CH...O interactions (shown in dashed red lines) mediated by {N1N2} moieties. (b) H-bonding interactions exhibited by {HP$_2$Mo$_5$} cluster anion in **1**. (c) Formation of zig-zag 2-D sheet through CH…O and π…π interactions (shown in dashed red and blue lines respectively) between neighboring 1-D chains. Four such chains are shown in blue, cyan, purple and yellow.
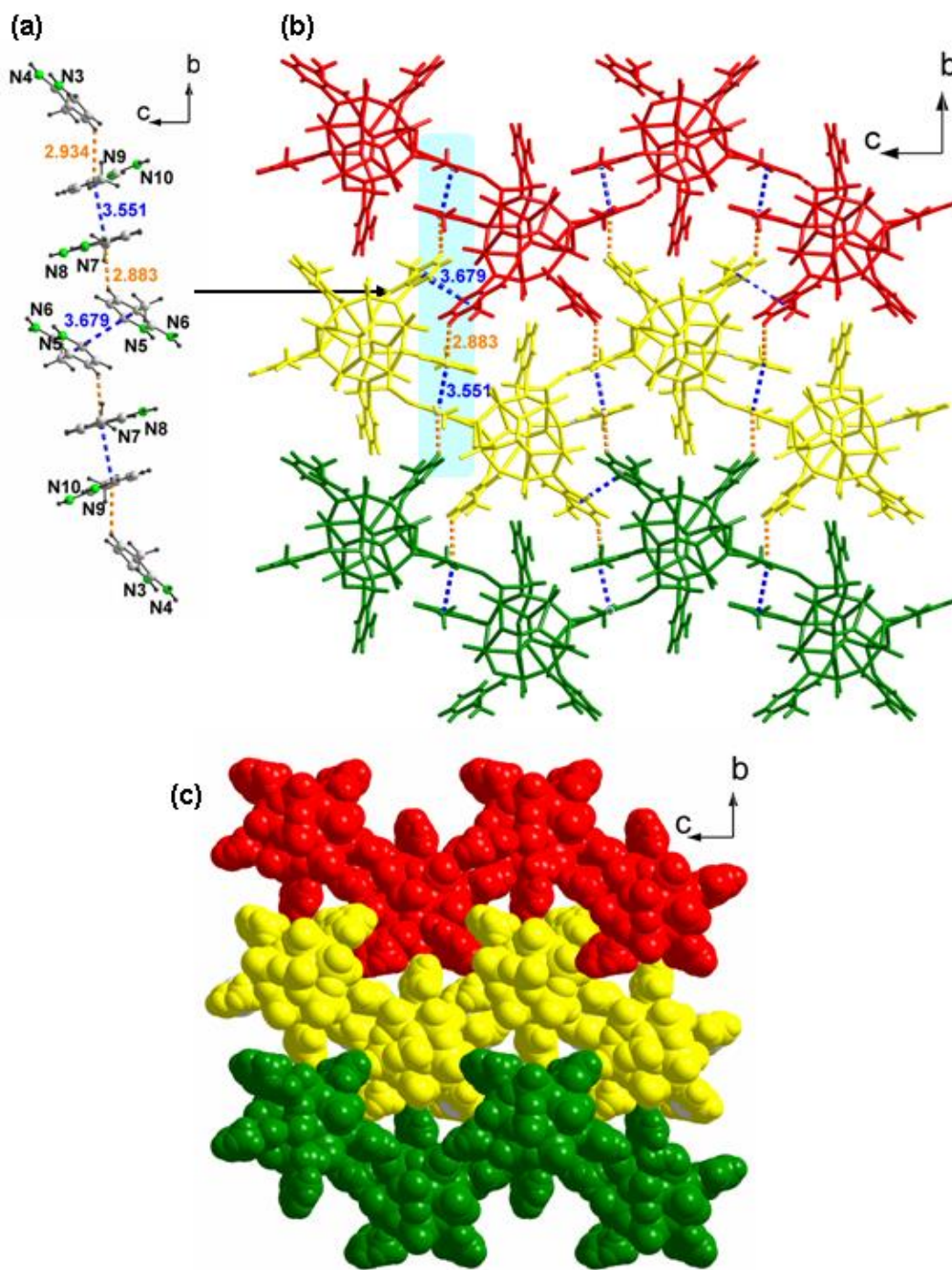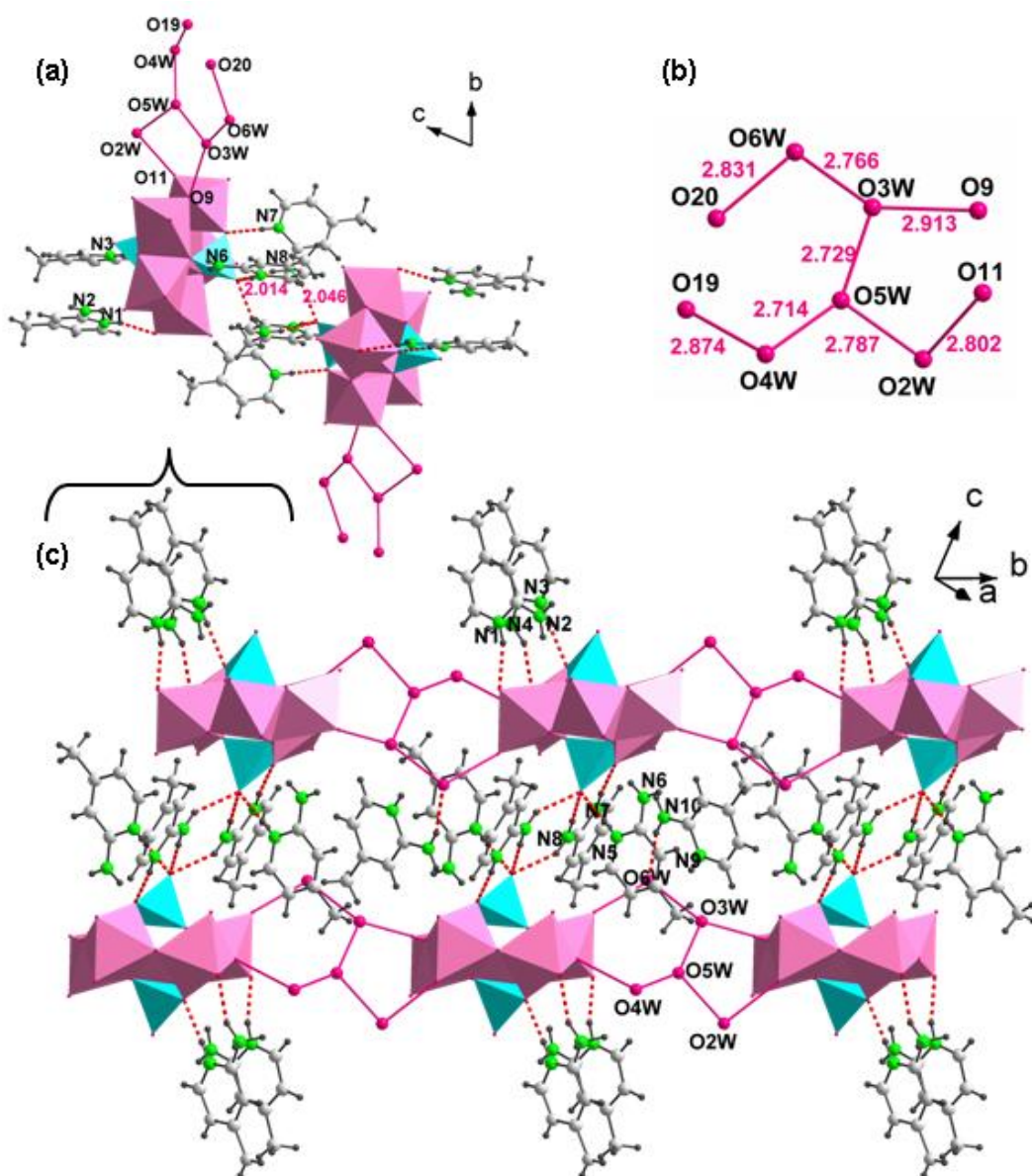
Figure II.3. (a) CH…π and π...π interactions (shown in dashed orange and blue lines) form a octameric unit. (b) Crystal packing in **1** is facilitated by CH…π interactions between neighboring sheets. Three such sheets are shown in red, yellow and green. (c) CPK representation of **1** showing solvent accessible voids.

The crystal structure analysis of **2** suggests the formation of a dimeric unit of $\{HP_2Mo_5\}$ cluster anions linked via H-bonding interaction mediated by {N7N8} moiety. {N1N2}, {N3N4} and {N5N6} moieties along with five lattice water molecules are attached to the dimeric unit through NH…O and O…O interactions respectively (refer Table II.3 and II.4 for H-bonding and O…O interactions respectively). Each of the dimers is further connected through pentameric water cluster to form 1-D chains which propagate along *b* axis as shown in Figure II.4c. The packing resulted in voids which are occupied by {N9N10} moieties. The occurrence of {N9N10} moieties in the voids is induced by the pentameric water cluster through O6W (N10H10A…O6W: 2.131(6) Å). Inter-chain H-bonding interaction mediated by {N5N6} moiety (N6H6B…O16: 2.127(5) Å) results in 2-D sheet in *ab* plane. Unlike in **1**, CH…π interactions between neighboring chains facilitated the packing of 1-D chains in **2**. The 2-D sheets are stacked parallel to each other along the *c* axis through lattice water molecule, O1W.

Table II.3. Hydrogen bonding interactions in **2**.

D-H…A	D-H (Å)	H…A (Å)	D…A (Å)	∠ D-H…A (°)
N1-H1…O21	0.859(8)	1.910(5)	2.742(9)	162.70(52)
N3-H3…O18	0.860(5)	1.960(5)	2.819(7)	175.31(29)
N4-H4A…O16	0.859(7)	2.061(5)	2.881(8)	159.45(40)
N5-H5…O23	0.861(5)	1.793(4)	2.647(7)	171.18(34)
N7-H7…O13	0.861(4)	2.010(6)	2.863(8)	171.06(26)
N8-H8A…O23	0.860(4)	2.014(6)	2.860(9)	167.62(27)

Figure II.4. (a) Dimeric unit in **2** wherein {HP$_2$Mo$_5$} cluster anions are linked through H-bonding (shown in dashed red lines) mediated by {N7N8} moiety. The pentameric water cluster is anchored to the dimer through O…O interactions shown in solid red lines. (b) The pentameric water cluster in **2**. (c) Dimer units linked through water clusters to form 1-D chain propagating along *b* axis. The 1-D chains result in voids which are occupied by {N9N10} moieties.
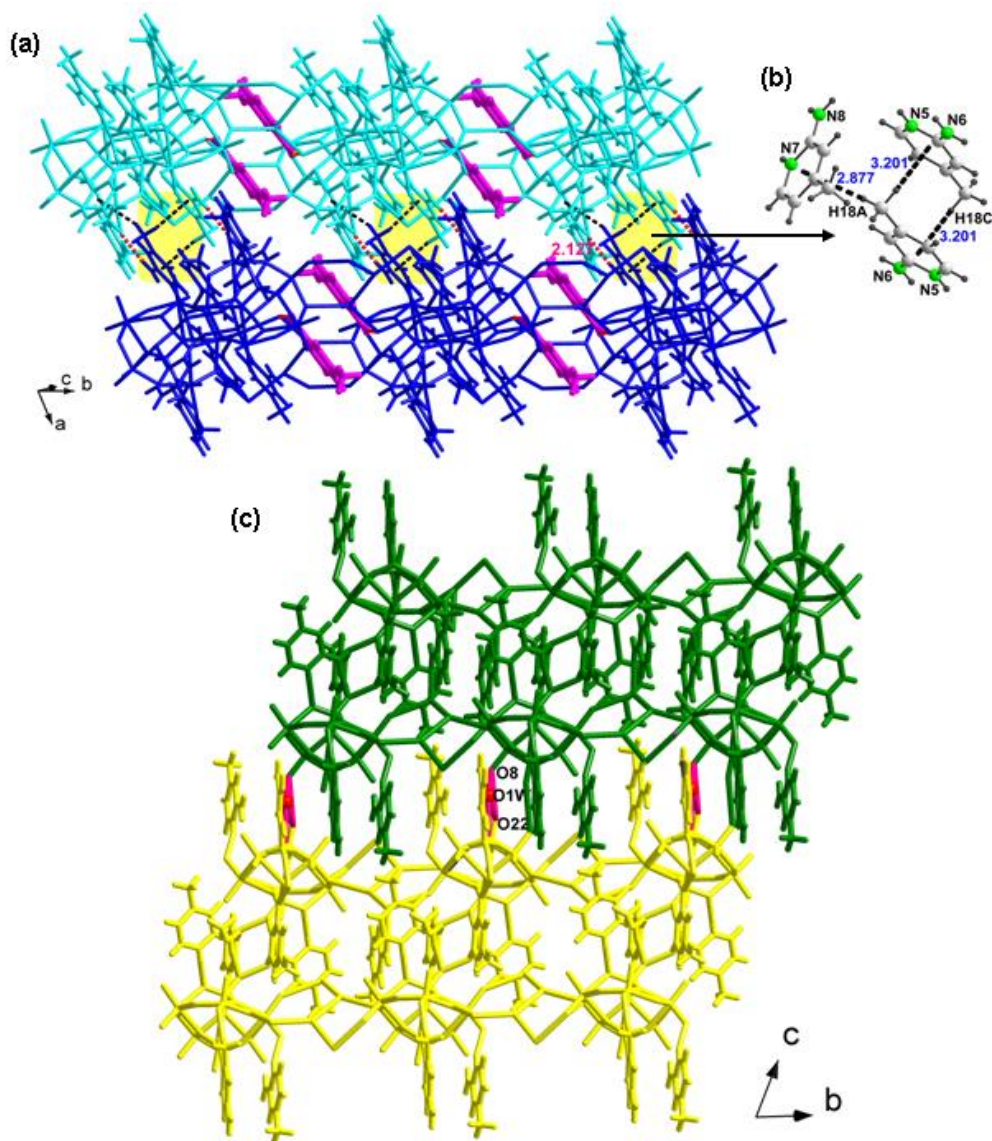
Figure II.5. (a) The connection between chains through H-bonding interaction (N6H6B…O16: 2.127(5) Å) and CH…π interactions to form a sheet. Two such chains are shown in cyan and blue. The voids in 1-D chains are occupied by {N9N10} moieties shown in purple color. (b) CH…π interactions in **2** are shown in dashed black lines. (c) Neighboring 2-D sheets (shown in green and yellow) are further linked by lattice water molecule, O1W to form a 3-D supramolecular network. O…O interactions are shown in solids red lines (refer Table II.3 for O…O interactions).

Table II.4. O…O interactions in **2**.

Sl. No.	O…O	Distance (Å)
1	O2W…O11	2.802(13)
2	O2W…O5W	2.787(16)
3	O3W…O9	2.913(9)
4	O3W…O5W	2.729(15)
5	O3W…O6W	2.766(12)
6	O4W…O5W	2.714(14)
7	O4W…O19	2.874(12)
8	O6W…O20	2.831(9)
9	O1W…O22	3.068(9)
10	O1W…O6	2.814(6)
11	O1W…O8	3.019(8)

II.3.2. Analysis of solids 1 and 2

FTIR spectra of **1** and **2** showed bands in the region 650-690, 750-830 and 900-930 cm^{-1} which are characteristic of molybdenum oxygen stretching. Bands at 1000-1100, 1400-1420 and 1620-1640 cm^{-1} were assigned to P-O stretching, N-H bending and C-H bending vibrations respectively [37]. In addition, FTIR spectrum of **2** showed bands at 3100-3400 cm^{-1} which could be attributed to O-H stretching (Figure II.6). SEM images of **1** and **2** showed the formation of well defined elongated needles and block-like morphology respectively (refer Figure II.7).
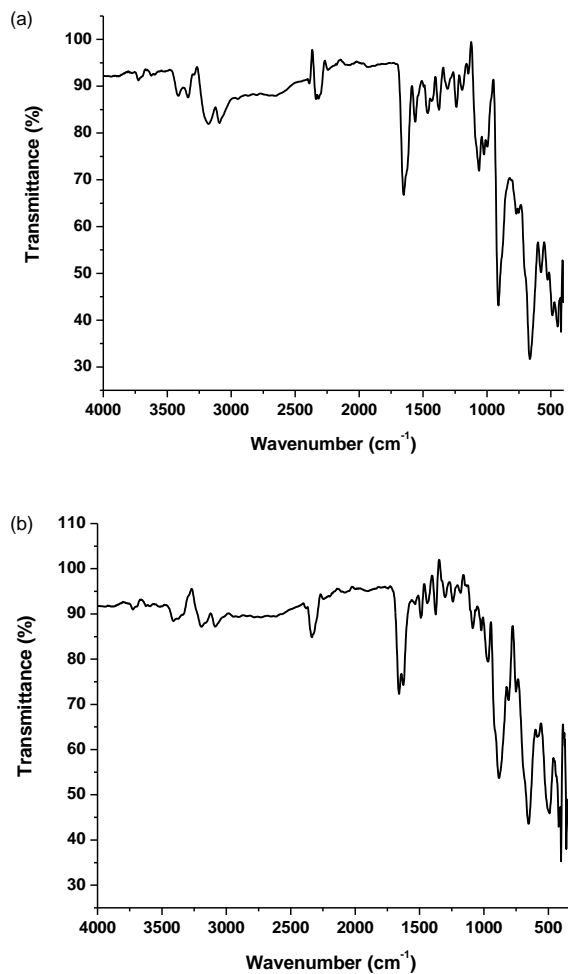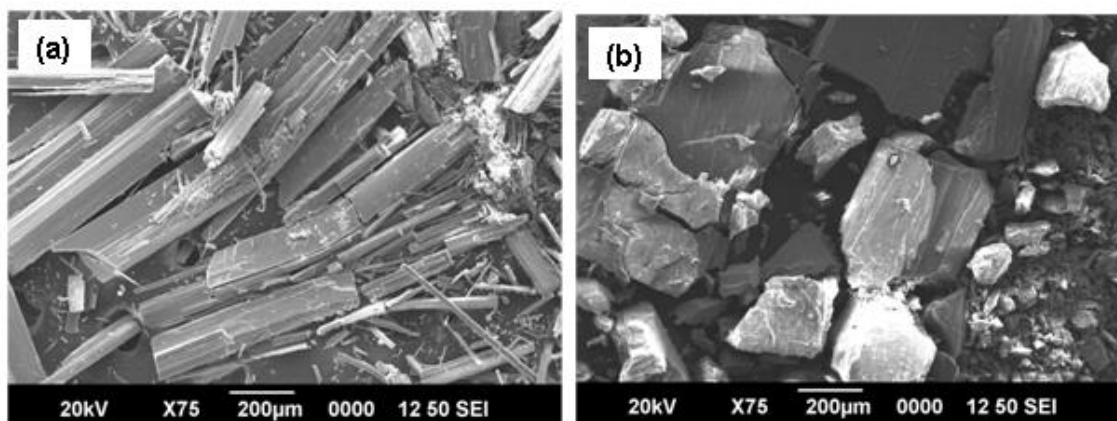
Figure II.6. FTIR Spectrum of (a) **1** and (b) **2**.

Figure II.7. SEM images of (a) **1** and (b) **2**.

TG analysis of **1** and **2** (Figure II.8) showed weight loss in two and three steps respectively. In **1**, the first weight loss upto 350ºC corresponding to 36.7% was due to the thermal degradation of five organic moieties. The second weight loss upto 800ºC could be assigned to the decomposition of {HP_2Mo_5} cluster anion. On the contrary, **2** showed an initial weight loss of 1.1 % at 100°C corresponding to loss of one water molecule. The loss of remaining water molecules along with protonated organic moieties was observed at slightly higher temperature (upto 350°C), as water molecules formed a pentameric water cluster in **2**. The third weight loss could be attributed to the decomposition of {HP_2Mo_5} cluster anion. In both **1** and **2**, the phase purity of the solids was established by comparing the experimental PXRD pattern with simulated powder pattern of the single crystal structure as shown in Figures II.9-II.10.
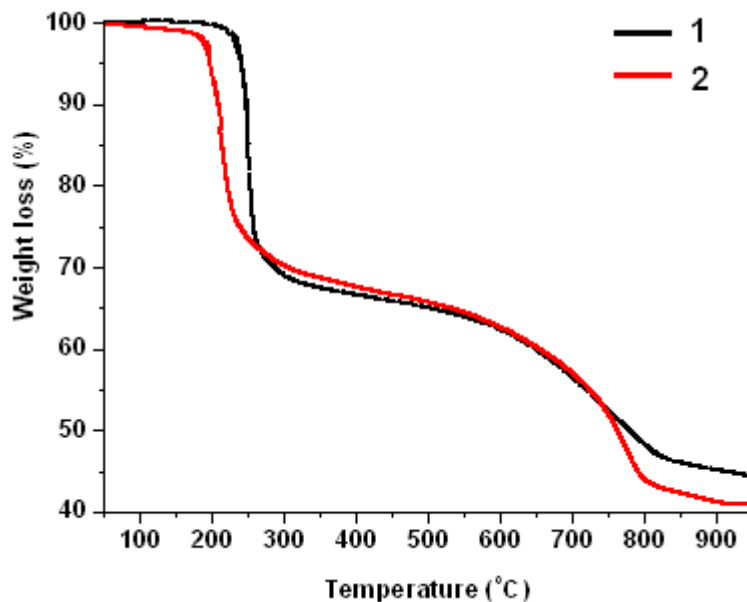
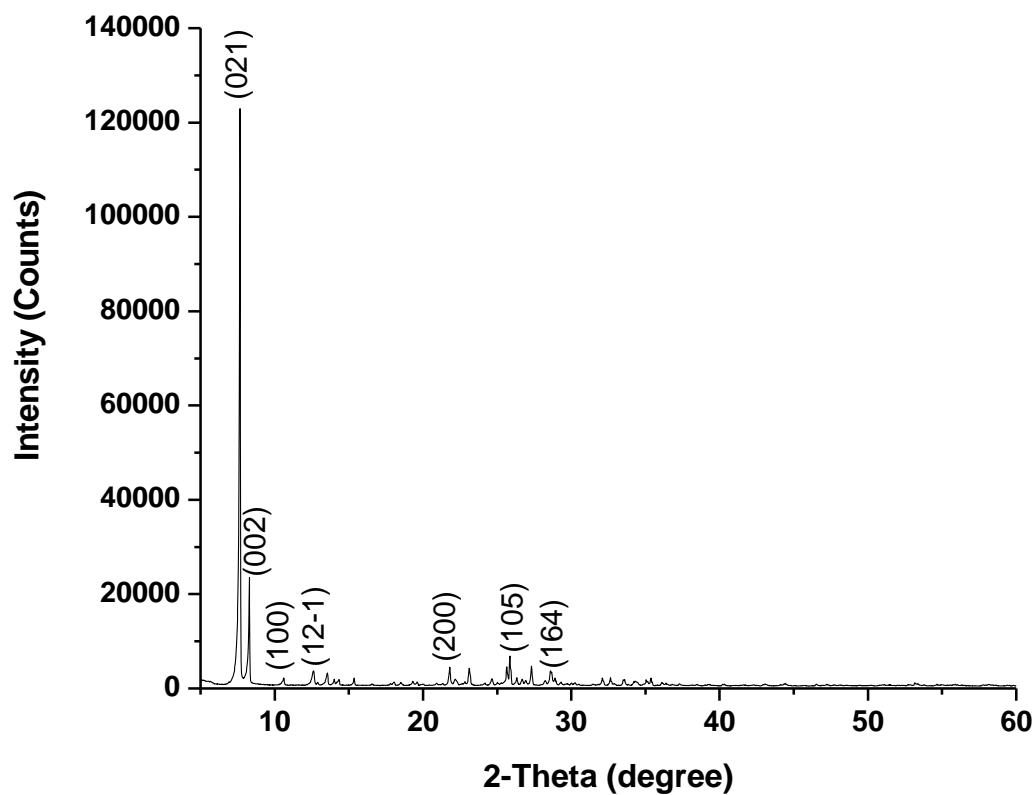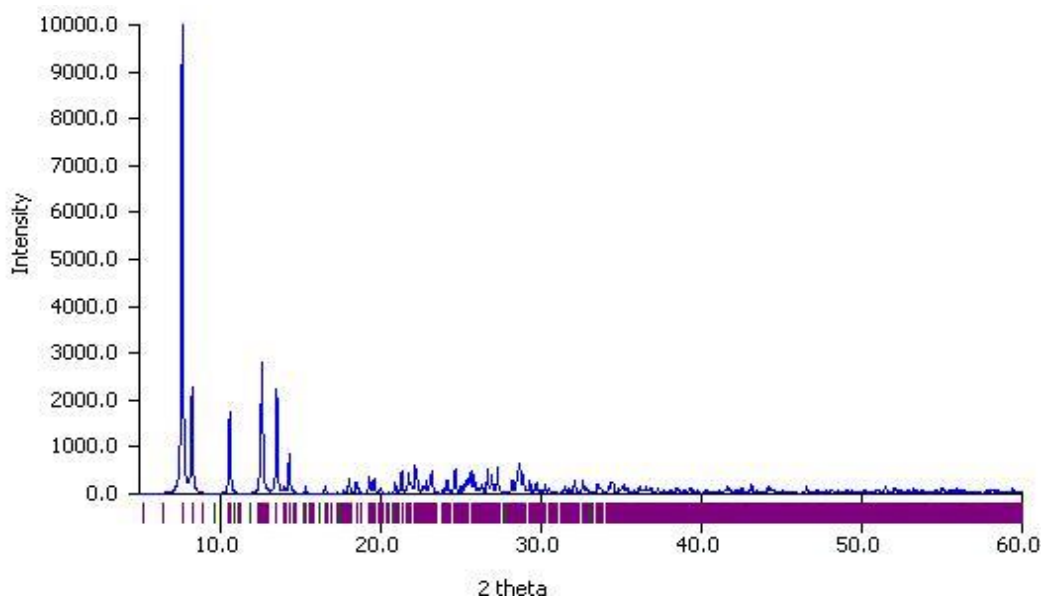**Figure II.8.** TGA curve of **1** and **2**.

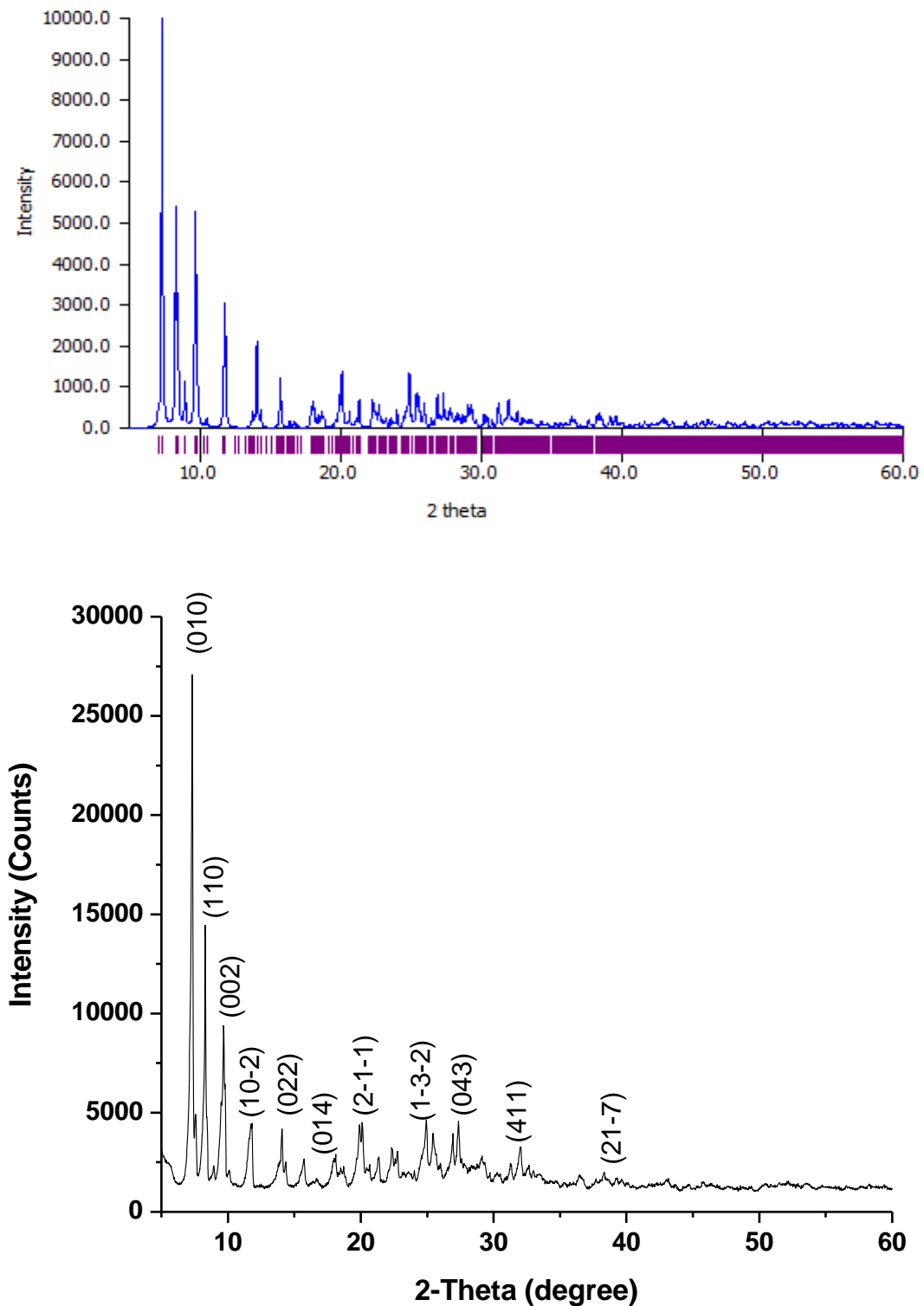**Figure II.9.** Simulated (top) and Experimental (bottom) PXRD of **1**.

Figure II.10. Simulated (top) and Experimental (bottom) PXRD of **2**.

II.3.3. Electrochemical behavior

The redox behavior of the solids was investigated using cyclic voltammetry in 1 mM $K_4[Fe(CN)_6]$ with a scan rate of 50 mVs^{-1}. In both **1** and **2**, two reversible waves (I-I' & II-II') were observed in the potential range between -0.2 and +0.8 V (Figure II.11a). The bare GCE gives a redox peak for $K_4[Fe(CN)_6]$ with mean peak potential E*1/2* = (*Epa* + *Epc*)/2 at 0.317 V which can be attributed to Fe^{II}/Fe^{III} [38]. The oxidation-reduction couple I-I' (+0.275 V and +0.279 V for **1** and **2** respectively) could be attributed to potassium ferrocyanide which shows a shift towards negative potential. The redox peak II-II' in **1** and **2** with half wave potentials +0.087 V and +0.072 V could be attributed to Mo^{VI}/Mo^V electron process. The slight deviations in the values can be ascribed to the different structural environment of $\{HP_2Mo_5\}$ clusters. The responses at +0.087 V and +0.072 V for solids **1** and **2** corresponding to Mo^{VI}/Mo^V electron process of the Strandberg cluster was further confirmed by comparing the cyclic voltammogram of the solid with that of the organic ligand used in its synthesis. For example, 2-amino-4-methylpyridine (*2a4mp*) is the organic ligand used for the synthesis of **2**. The value of E*1/2* = +0.275 V was observed for *2a4mp* which is quite distinct from the redox peaks detected for solid **2** corresponding to Fe^{II}/Fe^{III} and Mo^{VI}/Mo^V processes (refer Figure II.11).
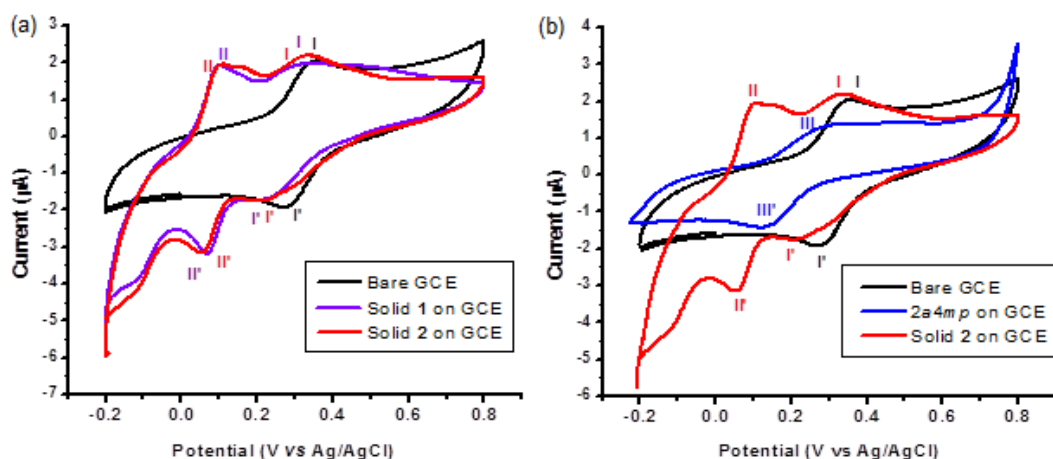
Figure II.11. (a) Cyclic voltammogram for **1** and **2** in the presence of 1 mM K$_4$[Fe(CN)$_6$] in 0.1 M KCl with a scan rate of 50 mVs^{-1}. (b) Comparison of voltammogram of 2*a*4*mp* with bare GCE and Solid **2**.

II.3.4. Band gap energy calculations

Optical band gap energy (E$_g$) of **1** and **2** were detrmined applying Kubelk- a–Munk (KeM or F(R)) function in Tauc method [39,40]. E$_g$ could be determined using Tauc method where (αhυ)^n is ploted against energy (hυ) in eV; here α is molar extintion coefficient. For solid powdered samples, often Kubelk- a–Munk (KeM or F(R)) is applied in Tauc method where the α is replaced by a function F(R) as given by equation (1); where R is the reflectance obtained from UV-Vis spectra.

$$F(R)=(1-R)^2/2R \quad \text{……………….}(1).$$

The plot F(R) v/s hυ(eV) when extrapolated on hυ axis gives the E$_g$ of the sample. The E$_g$ hence obtained is irrespective of transition (direct or indirect).

In order to obtain the E$_g$ with respect to the type of transition , the function F(R) is multiplied with hυ and raised to the power *n* corresponding to the type of transitions ((F(R) hυ)^n) which is then plotted against hυ(eV). For direct allowed transition, value of n=2 and

for indirect allowed transition, value of n=1/2. Figure below represents the plot of $F(R) h\upsilon)^2$ v/s $h\upsilon(eV)$ where direct allowed transition is determined.

Plots of $F(R)$ and $(F(R)h\upsilon)^n$ (where n = ½ and 2 for indirect allowed transition and direct allowed transition respectively) versus $h\upsilon(eV)$ for **1** and **2** are given in Figure II.12 and II.13 respectively. The optical band gap energies of solids **1** and **2** calculated from UV-DRS data has been tabulated in Table II.5. Although, the band gap energies are comparable in both the cases, a slight higher value is observed for solid **2.** The difference in band gap energy could be attributed to the difference in the nature of the isomeric ligands since the anion is monoprotonated in both cases.

Figure II.12. Plots of (a) Reflectance versus wavelength (b) F(R) versus $h\upsilon(eV)$, (c) $(F(R)h\upsilon)^{1/2}$ versus $h\upsilon(eV)$ and (d) $(F(R)h\upsilon)^2$ versus $h\upsilon(eV)$ for **1.**

Figure II.13. Plots of (a) Reflectance versus wavelength (b) F(R) versus hυ(eV), (c) (F(R)hυ)$^{1/2}$ versus hυ(eV) and (d) (F(R)hυ)^2 versus hυ(eV) for **2.**
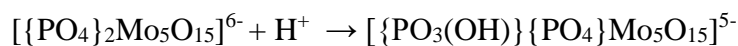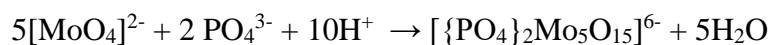
Table II.5. Table tabulates the irrespective, allowed indirect and allowed direct band gaps of **1** and **2**.

Solids	F(R) vs hυ (band gap energy irrespective of direct or indirect in eV)	[F(R) hυ]$^{1/2}$ (allowed indirect band gap energy in eV)	[F(R) hυ]^2 (allowed direct band gap energy in eV)
1	3.68	3.66	3.59
2	3.75	3.81	3.55

II.3.5. Chemistry of Formation

Solvent evaporation technique is one of the most facile methods employed for the crystallization of hybrid solids. The synthetic methodology used in the current study involves mixing of aqueous molybdate solution with organic ligand under constant stirring. However, mixing of the two solutions results in immediate precipitation of an amorphous solid. Therefore the solution is acidified using H_3PO_4 to obtain a clear solution. The latter when left undisturbed results in crystallization of solids **1** and **2**. The addition of H_3PO_4 has a two-fold effect. Firstly, it acts as a source of phosphate ions. Hence crystallization of PMO cluster based solids is facilitated. Secondly the pH of the reaction medium is adjusted to ~1. The highly acidic pH favors the formation of $\{HP_2Mo_5\}$ cluster anion [25] and results in protonation of the organic ligands (L). The formation of the solids can be visualized using the following equations wherein the Strandberg type polyoxometalate cluster is formed by protonation of tetrahedral molybdate; which under highly acidic conditions undergoes protonation:

$$5[MoO_4]^{2-} + 2\ PO_4^{3-} + 10H^+\ \rightarrow [\{PO_4\}_2Mo_5O_{15}]^{6-} + 5H_2O$$

$$[\{PO_4\}_2Mo_5O_{15}]^{6-} + H^+\ \rightarrow [\{PO_3(OH)\}\{PO_4\}Mo_5O_{15}]^{5-}$$

Initially, an electrostatic attraction between negativity charged $\{HP_2Mo_5\}$ cluster anion and positively charged organic moieties $(HL)^+$ initiates the self-assembly of solids **1** and **2**. The supramolecular assembly is further supported by secondary interactions which play a crucial role in crystal packing of these solids. Both the ligands have readily available $-NH_2$ and $-NH$ groups which induce H-bonding interactions between the cluster anions and $(HL)^+$ units. The presence of the aromatic ring in organic moieties ensures the possibility for $\pi...\pi$ and

CH…π interactions between (HL)$^+$ counter ions [41,42]. Therefore, the role of H-bonding, π…π and CH…π interactions in crystal packing in **1** and **2** seems obvious. Additionally, the crystal structure of **2** also showed the presence of lattice water molecules. Earlier we have demonstrated in several examples that aggregation of water cluster is a secondary factor in the crystal packing of such complex structures [27]. Protonation of Strandberg-type cluster anion [1] and synthesis under ambient conditions [25] are the key factors responsible for the aggregation of water molecules in PMO cluster based solids. Strikingly, of the two solids, only **2** favored the formation of a pentameric water cluster. This could be attributed to directionality of substituents on the organic ligands. While, the hydrophobic methyl group is in close proximity to the amino group in 2*a3mp*, the comparatively distant position of methyl group in 2*a4mp* allows –NH$_2$ group to form H-bond with lattice water molecules in **2**. Therefore, aggregation of water cluster is induced in **2**.

II.4. Conclusions

Two new Strandberg-type cluster based solids *viz.* {H-2*a3mp*}$_5$[{PO$_3$(OH)}{PO$_4$}Mo$_5$O$_{15}$], **1** and {H-2*a4mp*}$_5$[{PO$_3$(OH)}{PO$_4$}Mo$_5$O$_{15}$].6H$_2$O, **2** were successfully synthesized and characterized. Detailed structural analysis revealed the role of supramolecular interactions in the crystal packing of these solids. In addition, the formation of pentameric water cluster in **2** was rationalized on the basis of supramolecular interactions and directionality of substituents on the organic ligands. Further, the electrochemical nature of **1** and **2** was explored by means of three electrode system using 1 mM K$_4$[Fe(CN)$_6$] in 0.1 M KCl as supporting electrolyte. To the best of our knowledge the redox behavior of {P$_2$Mo$_5$} cluster based solids in the presence of K$_4$[Fe(CN)$_6$] has not been examined so far. The facile synthetic methodology used for the preparation of solids **1** and **2** can be successfully applied

for the crystallization of new hybrid solids based on Strandberg-type cluster anion. Moreover, a careful selection of the organic counterpart can modify electrochemical behavior along with porosity in hybrid solids. The optical band gap energies of the solids showed slight difference on account of their difference in the nature of the ligands.

References

1. Upreti, S.; Ramanan, A. *Cryst. Growth Des.* **2006**, 6, 2066-2071.

2. Shi, S.; Chen, L.; Zhao, X.; Ren, B.; Cui, X.; Zhang, J. *Inorg. Chim. Acta* **2018**, 482, 870-877.

3. Pathan, S.; Patel, A. *Catal. Sci. Technol.* **2014**, 4, 648-656.

4. Li, C.; Mizuno, N.; Yamaguchi, K.; Suzuki, K. *J. Am. Chem. Soc.* **2019**, 141, 7687-7692.

5. Xun, S.; Guo, T.; He, M.; Ma, R.; Zhang, M.; Zhu, W.; Li, H. *J. Colloid Interface Sci.* **2019**, 534, 239.

6. Joseph, J.; Radhakrishnan, R. C.; Johnson, J. K.; Joy, S. P.; Thomas, J. *Mater. Chem. Phys.* **2020**, 242, 122488-122496.

7. Abu, Z. B. M.; Farrag, A. A. A.; Asiri, A. M. *Powder Technol.* **2013**, 246, 643-649.

8. Lu, L.; Xie, Y. *J. Mater. Sci.* **2018**, 54, 4842-4858.

9. Manivel, A.; Anandan, S. *J. Solid State Electrochem.* **2011**, 15**,** 153-160.

10. Liu, J.; Wang, J.; Chen, M.; Qian, D. *J. Nanopart. Res.* **2017**, 19**,** 264-275.

11. Niu, J.; Ma, J.; Zhao, J.; Ma, P.; Wang, J. *Inorg. Chem. Commun.* **2011**, 14, 474-477.

12. Ma, X.; Zhou, F.; Yue, H.; Hua, J.; Ma, P. *J. Mol.Struct.* **2019**, 1198, 126865-126872.

13. Li, Z. L.; Wang, L. C.; Wang, J. P.; You, W. S.; Zhu, Z. M. *Dalton Trans.* **2014**, 43, 5840-5846.

14. Strandberg, R. *Acta. Chem. Scand.* **1973**, 27, 1004-1018.

15. Shi, Z.; Li, F.; Zhao, J.; Yu, Z. Y.; Zheng, Y.; Chen, Z.; Guo, Q.; Zhang, G.; Luo, Y. *Inorg. Chem. Commun.* **2019**, 102, 104-107.

16. Ji, Y. M.; Zhao, M.; Han, P. P.; Fang, Y.; Han, Q. X.; Li, M. X. *Inorg. Nano-Met. Chem*. **2018**, 48, 421-425.

17. Xu, M.; Li, F.; Wang, T.; Xu, L. *Inorg. Chem. Commun*. **2018**, 94, 123-126.

18. Zhao, H.; Li, J.; Fang, Y.; Chang, B.; Meng, Q.; Li, M.; Wang, C.; Zhu, X. *Bioorg. Med. Chem. Lett*. **2020**, 30, 126781-126786.

19. Ganesan, S. V.; Natarajan, S. *J. Chem. Sci.* **2005**, 117, 219-226.

20. Upreti, S.; Ramanan, A. *Synth. React. Inorg. Metal-org. Nano-Metal Chem.* **2008**, 38, 69-75.

21. Yan, D.; Zheng, L.; Zhang, Z.; Wang, C.; Yuan, Y.; Zhu, D.; Xu, Y. *J. Coord. Chem.* **2010**, 63, 4215-4225.

22. Ma, F. X.; Chen, Y. G.; Yang, H. Y.; Dong, X. W.; Jiang, H.; Wang, F.; Li, J. H. *J. Cluster. Sci*. **2019**, 30, 123-129.

23. Paul, L.; Dolai, M.; Panja, A.; Ali, M. *New J. Chem.* **2016**, 40, 6931-6938.

24. Qu, M.; Feng, H.; Ma, C.; Yang, Y.; Yu, X. *Inorg. Chem. Commun*. **2017**, 81, 22-26.

25. Joshi, A.; Gupta, R.; Singh, B.; Sharma, D.; Singh, M. *Dalton Trans*. **2020**, 49, 7069-7077.

26. Asnani, M.; Kumar, D.; Duraisamy, T.; Ramanan, A. *J. Chem. Sci.* **2012**, 124, 1275-1286.

27. Wang, Y.; Zhang, L. C.; Zhu, Z. M.; Li, N.; Deng, A. F.; Zheng, S. Y.; *Transition Met. Chem*. **2011**, 36, 261-267.

28. Thomas, J. Ph.D. Thesis, Indian Institute of Technology, Delhi, India, **2010**.

29. Zhai, Q.; Wu, X.; Chen, S.; Chen, L.; Lu, C. *Inorg. Chim. Acta* **2007**, 360, 3484-3492.

30. Harchani, A.; Haddad, A. *J. Clust. Sci*. **2015**, 26, 1645-1653.

31. Song, L.; Yu, K.; Su, Z.; Wang, C.; Wang, C.; Zhou, B. *J. Coord. Chem.* **2014**, 67, 522-532.

32. Bruker Analytical X-ray Systems, SMART: Bruker Molecular Analysis Research Tool,
    Version 5.618, **2000**.

33. Bruker Analytical X-ray Systems, SAINT-NT, Version 6.04, **2001**.

34. Bruker Analytical X-ray Systems, SHELXTL-NT, Version 6.10, **2000**.

35. Klaus B., University of Bonn, Germany DIAMOND, Version 4.1

36. Brown I D and Altermatt D **1985** Bond-valence parameters obtained from a systematic analysis of the Inorganic Crystal Structure Database *Acta Crystallogr*. **B41** 244.

37. Nakamoto K **1978** Infrared and Raman spectra of inorganic and coordination compounds (New York: John Wiley & Sons).

38. Jose, J.; Rajamani, A. R.; Anandaram, S.; Jose, S. P.; Peter, S. C.; Sreeja, P. B. *Appl. Organometal. Chem*. **2019**, e5063.

39. Lopez, R.; Gomez, R. *J. Sol-Gel Sci.Technol*. **2012**, 61, 1-7.

40. Reddy, K. M.; Manorama, S. V.; Reddy, A. R. *Mater. Chem. Phys*. **2003**, 78, 239-245.

41. Desiraju, G. R.; Vittal, J. J.; Ramanan, A. **2011**, Crystal Engineering - A Textbook (Singapore: World Scientific Publishing)

42. Das, D.; Biradha, K. *Austr. J. Chem.* **2019**, 72, 742-750.